INFLUENCE OF VERTICAL BREAKWATER WALL ROUGHNESS ON WAVE-INDUCED OVERTOPPING: A CFD-BASED STUDY

Le Quoc Huy⁽¹⁾, Le Duc Quyen⁽¹⁾, Tran Thi My Hong⁽²⁾

(1)The Viet Nam Institute of Meteorology, Hydrology and Climate Change (2)Ho Chi Minh City University of Technology, Viet Nam National University - Ho Chi Minh City

Received: 28/7/2025; Accepted: 15/8/2025

Abstract: In this study, we analyzed the wave dynamics in a nearshore region protected by a vertical breakwater through computational fluid dynamics (CFD) simulations. The focus was placed on evaluating the role of vertical wall roughness in influencing wave energy dissipation and overtopping behavior when waves encounter coastal structures. Four wall conditions were modeled with varying roughness coefficients: A smooth wall (NR = 0.0), and progressively rougher walls denoted as WR1 (0.5), WR2 (0.75), and WR3 (1.0). These cases were designed to systematically assess how increased surface roughness affects the hydrodynamic response of waves in front of and behind the breakwater. The simulation results demonstrated a clear trend: As wall roughness increased, the overtopping water depth consistently decreased. Specifically, the overtopping values were 0.083 m for the smooth wall (NR), followed by 0.082 m, 0.081 m, and 0.0719 m for WR1, WR2, and WR3, respectively. This suggests that increased wall roughness enhances wave energy dissipation, thereby reducing the volume of water overtopping the structure. These findings highlight the critical role of structural surface characteristics in coastal defense design. Incorporating surface roughness into vertical breakwater modeling can contribute to more effective wave energy attenuation, potentially improving the resilience and performance of coastal protection systems under wave impact.

Keyword: Vertical wall, overtopping, VoF model, Stokes wave.

1. Introduction

Wave characteristics near coastal regions are topics of great interest and importance to coastal engineering and oceanography. Waves, primarily generated by wind and natural forces, have the potential to cause erosion, coastal flooding, and damage to coastal infrastructure and ecosystems [1-5]. Wave height reduction approaches, which include strategies such as submerged structures and breakwaters, have explored the potential of various configurations such as submerged panels, breakwaters, porous structures, and perforated screens. Strategic placement of these structures dissipates wave energy, reducing wave heights and protecting coastal areas [6-8].

Natural features like vegetation reduce wave

Corresponding author: Tran Thi My Hong E-mail: tranthimyhong@hcmut.edu.vn

height such as mangroves, salt marshes, and other plants along the coast not only help the environment, but they also help to spread and absorb waves [9-12].

New methods have been created to deal with this problem, such as using air bladder systems and submerged floating cylinders. These methods, by injecting air bubbles or using floating structures, aim to disrupt wave propagation and reduce wave height by dissipating wave energy [13-16].

Extreme weather events can generate large waves, and when the height of incoming waves exceeds the crest elevation of a coastal or hydraulic structure, wave overtopping occurs. Such extreme waves have been responsible for significant damage to both offshore and nearshore structures due to the enormous impact forces produced by wave impingement [17], [18]. When waves break directly on a

vertical-faced coastal structure, they produce impact (or shock) pressures characterized by extremely high intensity and much shorter duration compared to non-breaking waves, which can lead to structural damage and surface erosion over time [19]. If the wave energy and height are sufficiently large, water may overtop the structure crest, resulting in overtopping waves and associated hazards.

Overtopping occurs when incident waves exceed the beach freeboard, allowing a significant volume of water to cross coastal dunes or structures and inundate previously protected areas. This phenomenon has been extensively studied to inform the design and optimization of coastal defense systems, such as dikes, seawalls, and revetments [20-26]. Accurately estimating wave overtopping is essential for improving coastal risk management strategies, particularly those aimed at mitigating flood-related hazards and storm surge impacts in vulnerable regions [27].

Wave overtopping plays a critical role in coastal erosion processes, as the forceful flow of water over structural crests can mobilize and transport sediment, ultimately destabilizing the shoreline and contributing to long-term morphological changes [28-32]. Furthermore, the discharge of overtopped water onto adjacent land can inundate low-lying hinterlands, leading to significant damage to infrastructure, agricultural zones, and residential areas, while also posing direct risks to human safety [33-36].

In this study, wave behavior in front of vertical structures with varying surface roughness was analyzed through computational fluid

dynamics (CFD) simulations. The simulations were conducted using regular wave boundary conditions and were based on fourth-order Stokes wave theory. Four roughness conditions were modeled, with roughness coefficients ranging from 0.0 to 1.0 to represent increasing wall vertical. The results indicate that surface roughness has a noticeable effect on wave attenuation. While the reduction in wave height was relatively modest in the lower roughness cases, a significant decrease was observed when the roughness coefficient reached its maximum value (WR = 1.0). This suggests that high surface roughness contributes meaningfully to wave energy dissipation and can be a key factor in the design of effective coastal defense structures.

2. Method

The wave flume had a length of 8.5 m and a height of 0.6 m. The water level (h) was established at a height of 0.25 m. A structure of 0.2 min length and 0.3 min height was positioned at the coordinates (7.5, 0 m). In addition, a wave creation device was erected at the coordinates (0.2, 0 m). The grid was partitioned into two sections: A larger grid including the entire area, and a smaller grid focusing on the x values ranging from 7.2 m to 8.5 m and the y values ranging from 0 to 0.6 m (Figure 1). The mesh was created using a rectangular quadrilateral grid with a linear element order, resulting in a total of 37,340 nodes and 18,140 elements (Table 1).

2.1. Computational fluid dynamics

The numerical model uses the incompressible RANS equations to express the motion of a fluid consisting of a mass conservation Equation (1) and a momentum conservation Equation (2).

$$\frac{\partial u_i}{\partial x_i} = 0 \tag{1}$$

$$\frac{\partial \rho u_i}{\partial t} + \frac{\partial \rho u_i u_j}{\partial x_j} - \frac{\partial}{\partial t} \left[\mu_{ef} \frac{\partial u_i}{\partial x_j} \right] = -\frac{\partial p}{\partial x_j} + \Gamma \tag{2}$$

$$\frac{\partial k}{\partial t} + U_j \frac{\partial k}{\partial x_j} = P_k - \beta k \omega + \frac{\partial}{\partial x_j} \left[\left(\nu + \sigma_j \nu_t \right) \frac{\partial k}{\partial x_j} \right] \tag{3}$$

Which t is the time, u_i (u=x,y) are the Cartesian components of the fluid velocity, ρ is the fluid density, μ_{ef} dynamic viscosity, and p is pressure, and Γ external body force. Turbulent effects are incorporated in the RANS equations (1) and (2) by solving one or more additional transport equations to yield a value for the turbulent kinematic viscosity and equation (3) where k is the turbulent kinetic energy, is the production term of, is the kinematic viscosity, ω is the specific dissipation rate, $\theta=0.09$ for a single fluid is the incompressible k- ω SST model;

2.2. Volume of fluid mode

Volume of fluid (VOF) model considered a

standard laboratory environment in which two phases of air and water phases (air primary phase and water secondary phase) to account for the water-air interaction in Computational fluid dynamics (CFD) wave flumes. The properties of these phases were as follows: ρ_f = 998.2 kg/m³, μ_f = 0.001 (kg/ms), ρ_a = 1.225 (kg/m³), and μ_a = 1.789*10-5 (kg/ms) Computational process cells containing both fluid phases are used to compute the mixture average density and viscosity using the following equation (4):

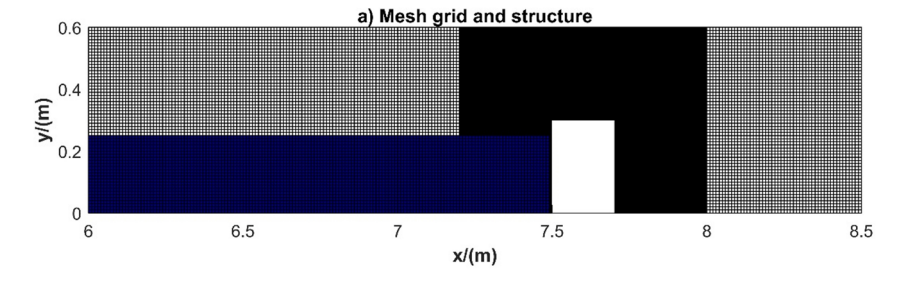
$$\begin{cases} \rho = \alpha_f \rho_f + (1 - \alpha_f) \rho_a \\ \mu = \alpha_f \mu_f + (1 - \alpha_f) \mu_a \end{cases} \tag{4}$$

Table 1. Properties generated mesh grid

Type meshing/ Method	Nodes	Elements	Average surface area (m²)	Element order	Grid size (m)
Rectangular/Quadrilaterals	37340	18140	1.77	Linear	0.02

Table 2. Wave boundary condition

Wave	Wave	Wave	Wave	Wave	Liquid	Ursell
theory	regime	height (H)	length (L)	steepness (H/L)	Depth (h)	Number H*L²/h³
4 th -order- Stokes	Shallow/ Intermediate	0.15	1.5	0.10	0.25	21.6



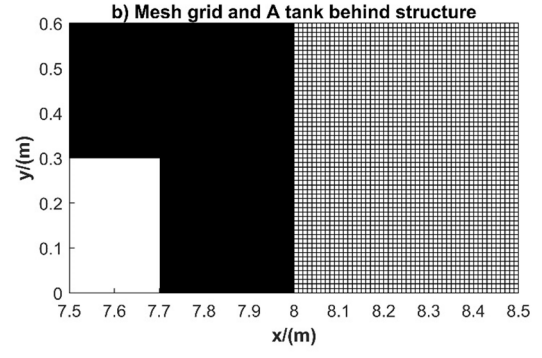


Figure 1. Mesh grid structure: a) mesh in the black area has a grid size of 0.01 m, with a coarser grid of 0.02 m, while the blue area indicates a water depth of 0.25 m. b) enlarge the tank located behind the structure

2.3. Theory wave Stokes

A numerical model was used to simulate the propagation of waves in a wave field with shallow to intermediate water depths. At the inlet boundary, we established the initial wave conditions with a wave height (H) of 0.15 m and wavelength (L) of 1.5 m (Table 2). We utilized Stokes 4^{-th} theory in ANSYS Fluent to conduct a simulation of wave propagation and determine the value of the free surface height (ζ) as eq (5);

$$\zeta(X,t) = \frac{1}{k} \sum_{i=1}^{4} \sum_{j=1}^{i} b_{ij} \xi^{i} \cos(jk(x-ct))$$
 (5)

Where, $\xi = \pi H/2$, wave number $k=2\pi/L$, c is the wave celerity, and b_{ij} are constants explained in Fenton (1990) [37]. Wave properties should be set in terms of the Ursell number (HL^2/h^3) , relative wave height (H/h), wave steepness (H/L), and wave regime (h/L) within the stability and breaking limits to ensure that the wave

theory with shallow or intermediate water suitable (Table 2).

2.4. Roughness

Roughness-wall, it is essential to determine the roughness height (Ks) and the roughness constant. The lack of roughness suggests the walls have a smooth surface structure. To enhance the visibility of the roughness, adjust the roughness height (Ks) to a non-zero value., these characteristics are employed. The selection of a suitable roughness constant (Cs) is primarily determined by the specific type of roughness. The roughness constant (Cs = 0, 0.5, and 1.0) was selected to precisely reproduce the resistance values seen by Nikuradse for pipes with densely packed, uniform roughness caused by sand grains. This selection was made in combination with k-epsilon turbulence models. In this study, roughness parameters are defined as follows: NR = 0, WR = 0.5, WR = 0.75, and WR = 1.0 for the roughness height (Ks) and roughness constant (Cs) (Table 3). Instead of utilizing physical roughness derived from finite elements.

Table 3. Roughness parameter

#	Case	Roughness height (K _s)	Roughness constant (C _s)
No.1	NR-0.0	0.0	0.0
No.2	WR-0.5	0.5	0.5
No.3	WR-0.75	0.75	0.75
No.4	WR-1.0	1.0	1.0

3. Result

3.1. Wave propagation process

Figure 2 shows a time-resolved sequence of water volume fraction contours that visually depict the evolution of wave propagation under different wall roughness conditions (WR = 0.0, 0.5, 0.75, and 1.0) from t = 0 s to t = 60 s. Each column (a to d) corresponds to a specific roughness case, while each row represents a snapshot at regular 10-second intervals, capturing the spatiotemporal changes in free surface profiles as waves interact with the vertical breakwater.

In the smooth-wall scenario (Column a, NR = 0.0), the initial condition at t = 0 s shows a flat free

surface with no visible perturbations. By t = 10.5 s, well-defined wave crests begin to emerge and propagate uniformly across the domain. These periodic waveforms remain coherent through subsequent frames, with minimal deformation observed up to t = 60 s. The high regularity and amplitude preservation throughout the column suggest negligible energy loss, which is consistent with the expectation for a smooth, non-resistant wall.

As roughness is introduced (Column b, WR = 0.5), wave behavior begins to deviate slightly from the smooth-wall case. Starting at t = 10.5 s, wave crests become evident, but their shape is less uniform. Over time, the crest lines become increasingly irregular, particularly noticeable

from t = 30.5 s onward. The water surface appears more disturbed, with minor reductions in wave height and increased turbulence along the wall interface, indicating moderate energy dissipation due to frictional effects.

This trend intensifies in Column c (WR = 0.75), where surface roughness further disrupts the wave structure. At early stages (e.g., t = 10.5 s), the waveforms already exhibit asymmetry and slight amplitude decay. As time advances, the crest-trough pattern loses uniformity, and the wave height visibly diminishes, especially in the later frames (t = 50.5 s to 60 s). The visual evidence supports stronger wave attenuation and disorganized flow near the wall, suggesting that increased roughness amplifies viscous and turbulent energy losses.

In Column d (WR = 1.0), which represents the highest roughness condition, wave deformation is most severe. From the onset of wave propagation, the free surface is characterized by fragmented wavefronts and irregular contours. The volume fraction contours indicate significant mixing and chaotic behavior close to the wall boundary. By $t=60\,\mathrm{s}$, the waveform is no longer clearly defined, with drastically reduced amplitude and disturbed flow fieldsclear evidence of maximal energy dissipation.

Overall. the figure demonstrates progressive transition from coherent, highenergy wave propagation in the smooth-wall case to severely damped, irregular motion in the roughest scenario. The contours reveal how increasing wall roughness intensifies viscous damping, disrupts the organized structure of wave crests and troughs, and reduces the capacity of the wave to retain energy during propagation. These findings reinforce the critical role of structural surface characteristics in coastal engineering design, particularly in enhancing the energy dissipation capacity of vertical breakwaters and reducing overtopping risk in nearshore environments.

3.2. Influent roughness

Figure 3-a, d presents the wave reflection characteristics under different wall roughness

conditions. corresponding to roughness coefficients of NR = 0.0 (smooth wall), WR = 0.5, WR = 0.75, and WR = 1.0. At a fixed free surface elevation of 0.4 m, the significant wave height (Hs) observed for the cases of NR, WR = 0.5, and WR = 0.75 is approximately 0.21m. In contrast, for the highest roughness case (WR = 1.0), the free surface and significant wave height are slightly reduced to 0.39 m and 0.20 m, respectively, as shown in Figure 3-d. Throughout the 60-second simulation period, wave trains continuously propagate from the offshore boundary toward the vertical breakwater. As they encounter the structure, the reflected wave energy varies with surface roughness, represented by the wave reflection coefficient. It is evident from the results that both the roughness height (Ks) and the roughness constant (Cs) play key roles in modulating wave reflection behavior and energy dissipation near the wall. Notably, across all cases, the wave amplitude begins to decrease significantly after approximately 10 seconds of interaction with the structure. This trend is consistent regardless of the specific roughness coefficient, indicating the general influence of structural interference on wave energy decay. However, as the roughness level increases, the reduction in wave magnitude becomes more pronounced, particularly in front of the breakwater. This is attributed to enhanced turbulent interactions and frictional losses associated with higher roughness parameters. Furthermore, volume of water transmitted or overtopped beyond the wall also diminishes with increasing roughness, reinforcing the energy-dissipative effect of rough surfaces. These effects are clearly visualized in the contour sequences shown in Figure 3. Specifically, subfigures a-1 to a-7 correspond to the smooth wall case (NR = 0.0), b-1 to b-7 illustrate WR = 0.5, c-1 to c-7 represent WR = 0.75, and d-1 to d-7 correspond to WR = 1.0. These visualizations further emphasize the progressive attenuation and scattering of wave energy due to increased surface roughnes.

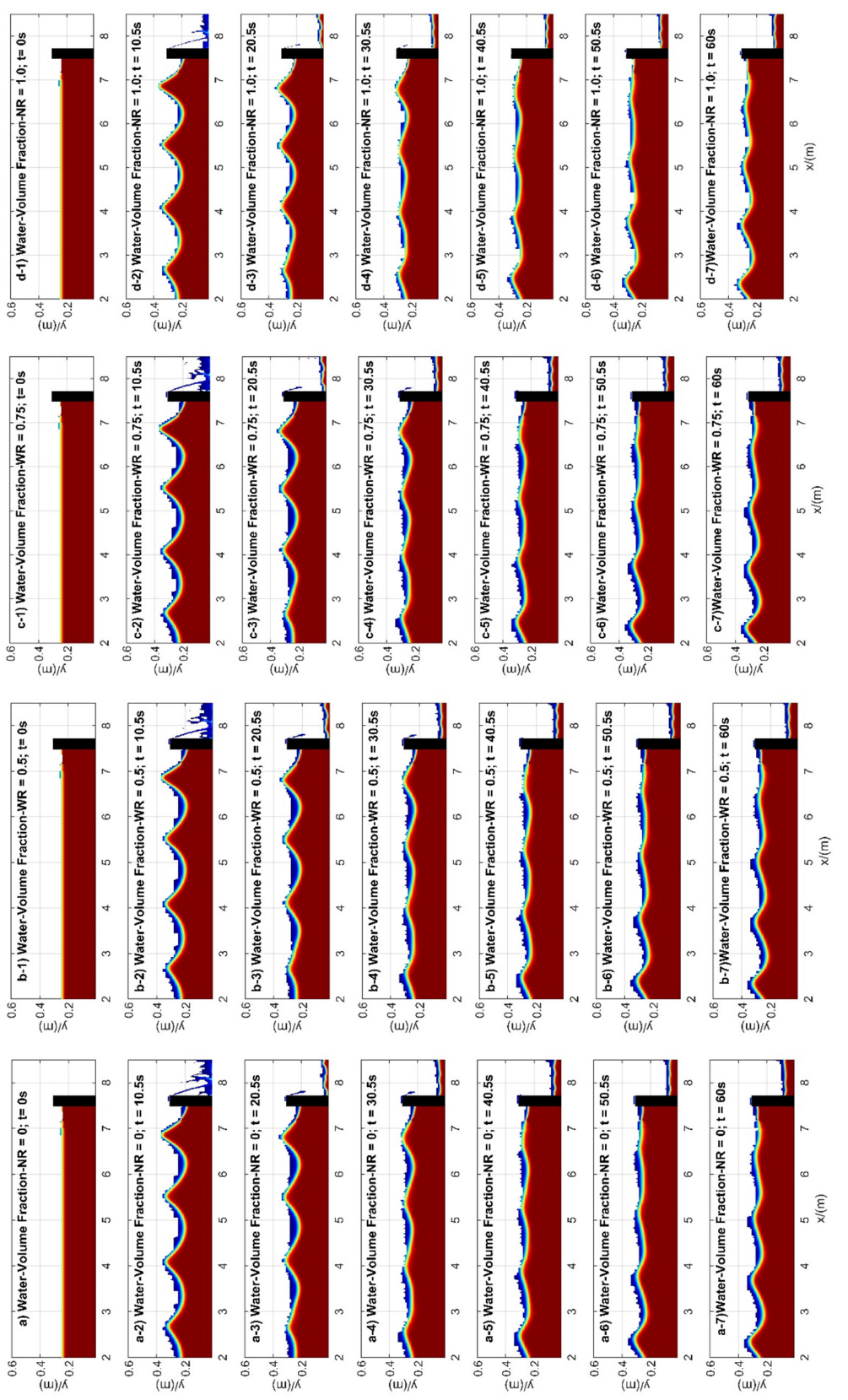


Figure 2. Wave propagation is instantaneous. a-1) to a-7) represent NR = 0, b-1) to b-7) correspond to WR = 0.5, c-1) to c-7) illustrate WR = 0.55, and d-1) to d-7) represent WR = 1.0

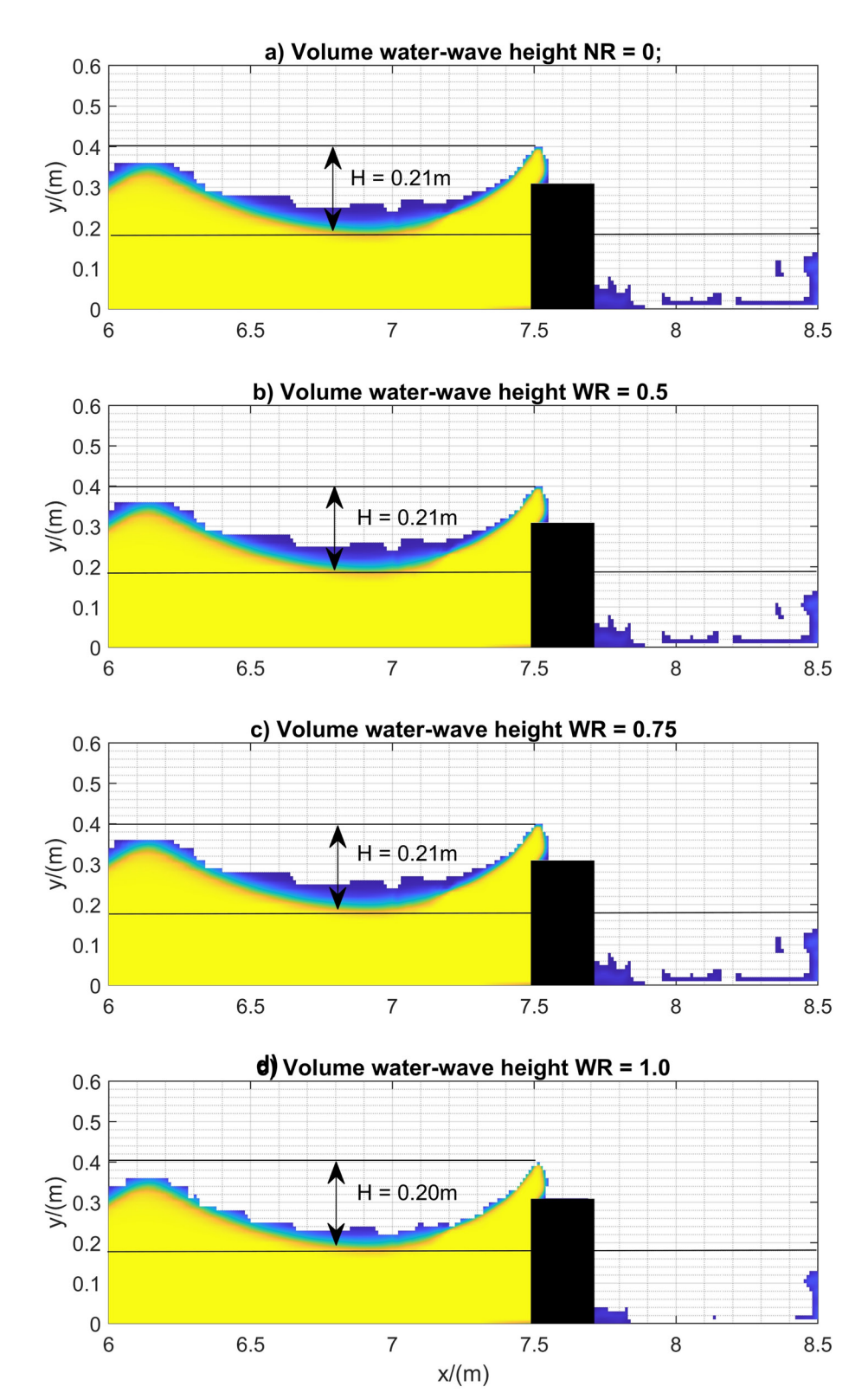


Figure 3. Free surface water (Volume fraction) height simulation. a) NR = 0, b) WR = 0.5, c) WR = 0.75, and d) WR = 1.0. The simulation is based on an incident wave with a significant wave height HO = 0.15 m, wave-length LO = 1.5 s, and still depth water h = 0.25 m

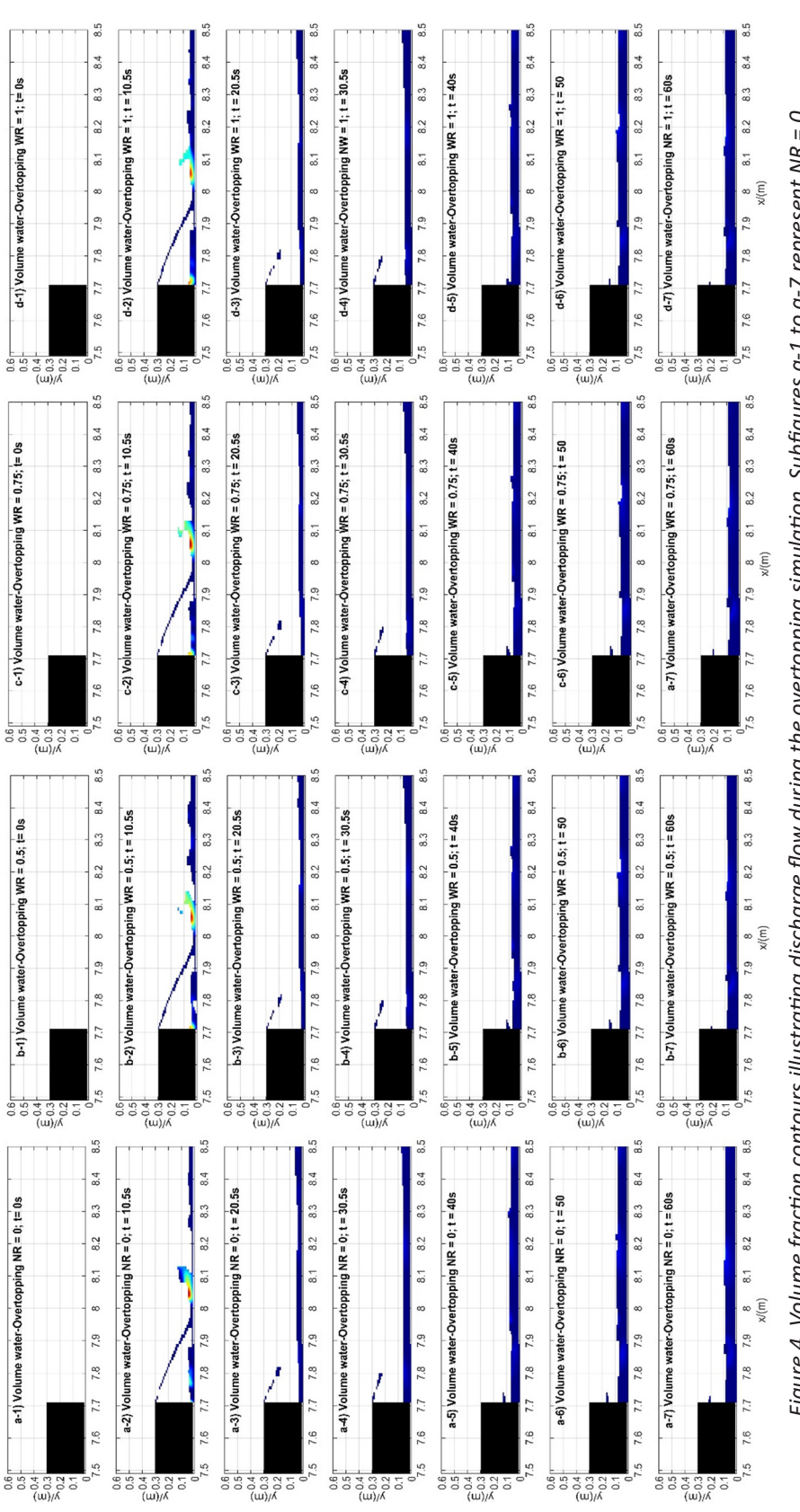


Figure 4. Volume fraction contours illustrating discharge flow during the overtopping simulation. Subfigures a-1 to a-7 represent NR = 0, b-1 to b-7 correspond to WR = 0.5, c-1 to c-7 illustrate WR = 0.75, and d-1 to d-7 depict WR = 1.0

Table 4. Total volume fraction of water overtopping the structure

#	Case	Water area (m)	
No.1	NR=0.0	0.0836	
No.2	WR=0.5	0.0820	(-1.98%)
No.3	WR=0.75	0.0815	(-1.97%)
No.4	WR=1.0	0.0719	(-1.86%)

3.3. Overtopping discharge estimates

Generally, most of the overtopping waves captured in the CFD simulations exhibit relatively small volumes, with only a small fraction of waves resulting in significantly larger overtopping events. The maximum volume of overtopping observed in a given sea state is influenced by several factors, including the mean overtopping discharge (Q) equation (6), the total wave duration, and the proportion of waves that contribute to overtopping. These parameters determine the collectively cumulative overtopping volume, which is a key metric in evaluating the performance of coastal protection structures. Figure 4 illustrates the post-structure overtopping region, modeled as a 2D tank with spatial boundaries defined by (x = 7.7 : 8.5 and y)= 0 : 0.6) discretized with a uniform grid spacing of 0.01 m. This results in a high-resolution computational mesh composed of (61*80) = 4880 cells. Each cell represents a volume element that is used to determine fluid presence through the Volume of Fluid (VOF) method.

$$Q_{total}$$
 = Number of cell * Grid spacing (6)

The total physical area of this domain is calculated as the number of cells multiplied by the cell area, yielding an overall overtopping evaluation domain of approximately 0.488 m. The VOF technique identifies water-filled cells with a volume fraction ($\alpha f = 1$), distinguishing them from air-filled cells where ($\alpha a = 0$).

This binary classification enables a precise quantification of overtopping water volumes under different surface roughness conditions. In the case of a smooth wall (NR = 0.0), 836 grid cells were identified as water-filled, resulting in a total overtopped area of 0.0836 m. As the wall roughness increased, a gradual reduction in overtopped area was observed. For WR = 0.5, the number of water-filled cells decreased to 820, corresponding to an overtopping area of 0.0820 m. At WR = 0.75, this number further reduced to 815 cells, or 0.0815 m. The lowest overtopping volume was recorded at the highest roughness level (WR = 1.0), with only 719 water-filled cells, equating to a significantly lower overtopped area of 0.0719 m (Table 4).

4. Conclusion

The CFD simulations varied the roughness coefficient with constants (NR = 0, WR = 0.5, WR = 0.75, WR = 1.0). These constants slightly impacted the wave characteristics in front of the vertical wall but not significantly. The difference became noticeable when the roughness coefficient reached its maximum value (WR = 1.0), where the recorded wave height was $0.2 \, \text{m}$ compared to $0.21 \, \text{m}$ in other cases.

Additionally, the variation in roughness parameters between cases can be observed through overtopping discharge. The results show that the water overtopping rate tends to decrease as the roughness coefficient increases: (NR = 0.0) 0.083 m, (WR = 0.5) 0.082 m, (WR = 0.75) 0.081 m, and (WR = 1.0) 0.0719 m.

Author Contributions: Conceptualization: Le Quoc Huy, Le Duc Quyen, Tran Thi My Hong; Data processing: Le Quoc Huy, Le Duc Quyen, Tran Thi My Hong; Methodology: Le Quoc Huy, Le Duc Quyen, Tran Thi My Hong; Writing - original draft: Le Quoc Huy, Le Duc Quyen, Tran Thi My Hong.

Declaration: The authors declare that this manuscript is their original research, has not been previously published, is not plagiarized or copied from other works, and that there are no conflicts of interest among the authors.

Acknowledgements: This publication is a result of the project "Research to determine the warning levels of natural disaster risks due to rising sea levels in some key coastal areas of Viet Nam" under grant number KC09.12/21-30 supported by the National Foundation for Science and Technology Development (NAFOSTED).

Reference

- 1. Hettiarachchi, S., and Samarawickrama, S. (2006), "The tsunami hazard in Sri Lanka strategic approach for the protection of lives, ecosystems and infrastructure", Coastal Engineering Journal, 48(03), 279-294.
- 2. Griggs, G., and Reguero, B. G. (2021), "Coastal adaptation to climate change and sea-level rise", Water, 13(16), 2151. https://doi.org/10.3390/w13162151.
- 3. Cochard, R. etal. (2008), "The 2004 tsunami in Aceh and Southern Thailand: a review on coastal ecosystems, wave hazards and vulnerability", Perspectives in Plant Ecology, Evolution and Systematics, 10(1), 3-40. https://doi.org/10.1016/j.ppees.2007.11.001.
- 4. Sutton-Grier et al. (2015), "Future of our coasts: The potential for natural and hybrid infrastructure to enhance the resilience of our coastal communities, economies and ecosystems", Environmental Science & Policy, 51, 137-148. https://doi.org/10.1016/j.envsci.2015.04.006.
- 5. Pascal, N. et al. (2016), "Economic valuation of coral reef ecosystem service of coastal protection: A pragmatic approach", Ecosystem services, 21, 72-80. https://doi.org/10.1016/j.ecoser.2016.07.005
- 6. Johnson, H. K. et al. (2005), "Modelling of waves and currents around submerged breakwaters", Coastal Engineering, 52(10-11), 949-969. DOI:10.1016/j.coastaleng.2005.09.011.
- 7. Carevic, D., Loncar, G., and Prsic, M. (2013), "Wave parameters after smooth submerged breakwater", Coastal engineering, 79, 32-41. https://doi.org/10.1016/j.coastaleng.2013.04.004.
- 8. Türker, U. (2014), "Excess energy approach for wave energy dissipation at submerged structures", Ocean engineering, 88, 194-203. DOI:10.1016/j.oceaneng.2014.06.030.
- 9. Augustin, L. N. et al. (2009), "Laboratory and numerical studies of wave damping by emergent and near-emergent wetland vegetation", Coastal Engineering, 56(3), 332-340. https://doi.org/10.1016/j.coastaleng.2008.09.004.
- 10. Anderson, M. E. et al. (2011), *Wave dissipation by vegetation*. Coastal and Hydraulics Laboratory Engineering Technical Report, ERDC/CHL TR-11-2.
- 11. Nowacki, D. J. et al. (2017), "Spectral wave dissipation by submerged aquatic vegetation in a backbarrier estuary", Limnology and Oceanography, 62(2), 736-753. https://doi.org/10.1002/lno.10456.
- 12. Hadadpour, S. et al. (2019), "Numerical investigation of wave attenuation by rigid vegetation based on a porous media approach", Journal of Coastal Research, 92(SI), 92-100. DOI:10.2112/SI92-011.1.
- 13. Deane, G. B., and Stokes, M. D. (2002), "Scale dependence of bubble creation mechanisms in breaking waves", Nature, 418(6900), 839-844.
- 14. Haberlin, D. et al. (2021), "Field and flume tank experiments investigating the efficacy of a bubble curtain to keep harmful jellyfish out of finfish pens", Aquaculture, 531, 735915. https://doi.org/10.1016/j.aquaculture.2020.735915.
- 15. van Gent, M. R. et al. (2022), "Wave overtopping discharges at rubble mound breakwaters including effects of a crest wall and a berm", Coastal Engineering, 176, 104151.
- 16. Mata, M. I., and van Gent, M. R. (2023), "Numerical modelling of wave overtopping discharges at rubble mound breakwaters using OpenFOAM®", Coastal Engineering, 181, 104274. https://doi.org/10.1016/j.coastaleng.2022.104274.
- 17. Hamoudi, B., and Varyani, K. S. (1998), "Significant load and green water on deck of offshore units/vessels", Ocean Engineering, 25(8), 715-731. https://doi.org/10.1016/S0029-8018(97)10005-1.
- 18. Ryu, Y., Chang, K. A., and Mercier, R. (2007), "Runup and green water velocities due to breaking wave impinging and overtopping", Experiments in Fluids, 43, 555-567. DOI:10.1007/s00348-007-0332-0.
- 19. Kirkgöz, M. S. (1990), "An experimental investigation of a vertical wall response to breaking wave

- impact", Ocean Engineering, 17(4), 379-391. https://doi.org/10.1016/0029-8018(90)90030-A.
- 20. Allsop, W. et al. (2005, September), "Wave overtopping at vertical and steep seawalls", In Proceedings of the Institution of Civil Engineers-Maritime Engineering (Vol. 158, No. 3, pp. 103-114). Thomas Telford Ltd. https://doi.org/10.1680/maen.2005.158.3.103.
- 21. Contestabile, P. et al. (2020), "Crown wall modifications as response to wave overtopping under a future sea level scenario: An experimental parametric study for an innovative composite seawall", Applied Sciences, 10(7), 2227. https://doi.org/10.3390/app10072227
- 22. EurOtop, I. I. (2018), Manual on wave overtopping of sea defences and related structures: An overtopping manual largely based on European research, but for worldwide application. European Overtopping Manual.
- 23. Koosheh, A. et al. (2022), "Experimental study of wave overtopping at rubble mound seawalls", Coastal Engineering, 172, 104062. https://doi.org/10.1016/j.coastaleng.2021.104062/
- 24. Lee, B. W. et al. (2019), "A hydraulic experimental study of a movable barrier on a revetment to block wave overtopping", Applied Sciences, 10(1), 89. https://doi.org/10.3390/app10010089.
- 25. Rubinato, M., Heyworth, J., & Hart, J. (2020), "Protecting coastlines from flooding in a changing climate: A preliminary experimental study to investigate a sustainable approach", Water, 12(9), 2471. https://doi.org/10.3390/w12092471.
- 26. van der Meer, J., and Bruce, T. (2014), "New physical insights and design formulas on wave overtopping at sloping and vertical structures", Journal of Waterway, Port, Coastal, and Ocean Engineering, 140(6), 04014025. https://doi.org/10.1061/(ASCE)WW.1943-5460.0000221.
- 27. Winter, G. et al. (2020), "Steps to develop early warning systems and future scenarios of storm wave-driven flooding along coral reef-lined coasts", Frontiers in Marine Science, 7, 199. https://doi.org/10.3389/fmars.2020.00199.
- 28. Kobayashi, N., and Wurjanto, A. (1989), "Wave overtopping on coastal structures", Journal of Waterway, Port, Coastal, and Ocean Engineering, 115(2), 235-251. https://doi.org/10.1061/(ASCE)0733-950X(1989)115:2(235).
- 29. Jiménez, J. A. et al. (2007), "Sediment transport and barrier island changes during massive overwash events", In Coastal Engineering 2006: (In 5 Volumes) (pp. 2870-2879).
- 30. Yuksel, Z. T., and Kobayashi, N. (2020), "Comparison of revetment and sill in reducing shore erosion and wave overtopping", Journal of Waterway, Port, Coastal, and Ocean Engineering, 146(1), 04019028. https://doi.org/10.1061/(ASCE)WW.1943-5460.0000543.
- 31. Luom, T. T. et al. (2021), "Using fine-grained sediment and wave attenuation as a new measure for evaluating the efficacy of offshore breakwaters in stabilizing an eroded muddy coast: Insights from Ca Mau, the Mekong Delta of Viet Nam", Sustainability, 13(9), 4798. https://doi.org/10.3390/su13094798.
- 32. Le Xuan, T. et al. (2022), "Evaluation of coastal protection strategies and proposing multiple lines of defense under climate change in the Mekong Delta for sustainable shoreline protection", Ocean & Coastal Management, 228, 106301. https://doi.org/10.1016/j.ocecoaman.2022.106301.
- 33. Gallien, T. W. et al. (2014), "Urban coastal flood prediction: Integrating wave overtopping, flood defenses and drainage", Coastal Engineering, 91, 18-28. DOI:10.1016/j.coastaleng.2014.04.007.
- 34. Xie, D. et al. (2019), "Coastal flooding from wave overtopping and sea level rise adaptation in the Northeastern USA", Coastal Engineering, 150, 39-58. https://doi.org/10.1016/j.coastaleng.2019.02.001.
- 35. Qiang, Y. et al. (2021), "Coastal town flooding upon compound rainfall-wave overtopping-storm surge during extreme tropical cyclones in Hong Kong", Journal of Hydrology: Regional Studies, 37, 100890. https://doi.org/10.1016/j.ejrh.2021.100890.
- 36. Lima, M. et al. (2023), "Wave Overtopping and Flooding Costs in the Pre-Design of Longitudinal Revetments", Water, 15(7), 1434. https://doi.org/10.3390/w15071434.
- 37. Fenton, J. (1985), "A fifth-order Stokes theory for steady waves", Journal of Waterway, Port, Coastal and Ocean Engineering 111.2 (1985): 216-234.